Two-fluid plasma model for ultrashort laser-induced electron-hole nanoplasmas

B. Morel,* R. Giust, K. Ardaneh, and F. Courvoisier†
FEMTO-ST Institute, Université Bourgogne-Franche-Comté, CNRS, 15B avenue des Montboucons, 25030 Besançon Cedex, France

(Received 7 February 2022; revised 1 June 2022; accepted 30 June 2022; published 28 July 2022)

We present a two-fluid plasma model to describe localized interaction, at submicrometer scale, of highly focused ultrashort laser pulses within dielectrics and semiconductors. This model includes transport of the electron-hole plasma, electron-hole scattering, photoionization, impact ionization, and interactions between charge carriers and phonons. We start with a plasma kinetic description, and we consistently derive the two-fluid plasma model equations. Our numerical results highlight that transport of the electron-hole plasma can strongly affect the plasma density profile in the case of extremely localized interaction.

DOI: 10.1103/PhysRevB.106.035207

I. INTRODUCTION

Ultrashort laser pulses are a powerful tool to induce modifications of materials [1–4]. Particularly in transparent dielectrics, ultrashort laser pulses can be used to locally modify, inside the material's bulk, the chemical structure, the index of refraction, and the density of color centers; photopolymerize; and generate nanogratings, surface nanostructures, or internal voids. A large number of application fields have benefitted from fundamental advances: surgery and biomedicine, photonics, microfluidics, and high-speed laser manufacturing [2,5–7].

Pushing forward these applications to nanometric structuring requires the support of numerical modeling [8]. Under laser-induced strong field, bound electrons transit from the valence band to the conduction band [1,9,10], leaving a hole in the valence band. Particles of the electron-hole plasma are accelerated in the laser field, which results in the multiplication of the free carrier density via impact ionization and potentially in the creation of a dense electron-hole plasma. Finally, at timescales much larger than several picoseconds, thermal and structural events take place inside the material [1]. Our model is focused on the plasma density buildup at timescales up to several picoseconds.

A large number of different models have been developed to study the propagation of ultrashort laser pulses ($\sim$100 fs) in the high-intensity regime ($\sim 10^{14}$ W/cm^2) inside dielectrics and subsequent ionization. These models can be classified into two groups. In the first, several models were developed to study the filamentation regime inside transparent solids with propagation scales on the order of several tens of micrometers [11,12]. Pulse propagation models, such as the unidirectional pulse propagation equation [13], are derived from Maxwell's equations and coupled with a rate equation for free-electron generation [14]. These models are well suited to describing the spatiotemporal evolution of the pulse under the different linear and nonlinear phenomena: Kerr and Raman effects, group velocity dispersion, diffraction, nonlinear ionization, plasma absorption, and recombinations. They can be refined to describe nonparaxial propagation [15,16]. However, the derivation of the pulse propagation equation requires assumptions of unidirectionality, local neutrality, and transverse fields. These assumptions are not well suited to the case of nanoplasmas (<1 μm) induced by tightly focused beams [3].

In the second group, the models are intended to describe energy deposition in dielectrics at the micrometric scale and are computationally very expensive because the full set of Maxwell equations is solved. Several descriptions of the plasma have been used: in Refs. [17–19], plasma formation and heating are described by rate equations. A more refined model is the single-fluid hydrodynamic approach [20,21]. An approach based on a two-temperature model was used in Ref. [22].

In these previous works, the transport phenomena were conventionally neglected since valence holes are conventionally heavy compared to the effective electron mass ($m_h^* = 5m_e$–$10m_e$) [21,23,24]. Because of Coulomb attraction, transport of electrons and holes remains quasi-identical. The fluid of the heaviest particle (the electron or hole) limits the transport of the lightest one. If the electron and hole have comparably light masses, then actual transport can be significant. Neglecting transport phenomena can therefore be inappropriate for materials with light holes such as sapphire [25], magnesium oxide [26], silicon [27], and zinc oxide [28]. Ultrafast transport at high speed (1.5×10^6 m/s) was recently observed experimentally in the latter material with pump-probe imaging ellipsometry [28]. A density-dependent two-temperature model was recently developed [29] and includes electron-hole transport in semiconductors. This model describes the evolution of free-carrier density, carrier temperature, lattice temperature, density, and energy transport but hypothesizes plasma neutrality and the same temperature for conduction electrons and valence holes.

Here, we propose a more general theoretical description of laser-induced excitation of dielectrics and semiconductors that takes into account the transport phenomena and hence is

*benoit.morel@femto-st.fr
†francois.courvoisier@femto-st.fr

valid for any effective mass ratio. We will particularly emphasize here the case where the mass ratio is around 1 since it is the case that differs most from the state of the art described above. In this case, we observed a significant transport and also important consequences resulting from the hole dynamics (modification of the cutoff frequency, additional impact ionization, warm holes). Our fluid model includes five-moment transport equations for each fluid, photoionization, impact ionization, electron-hole scattering, and interactions between carriers and phonons. The approach is valid only when the band structure of the material remains and is intended to describe the transient regime before the occurrence of nonthermal melting [30] or of the transformation of the plasma into warm, dense matter [31–33].

This paper is organized as follows: in Sec. II, we recall the two-fluid plasma model equations for an electron-hole plasma inside a band gap material with parabolic energy bands, and we briefly review the different physical phenomena included in the model. In Sec. III, we derive the source terms describing electron-hole scattering, interactions between carriers and phonons, photoionization, and impact ionization. Finally, in Sec. IV, our numerical results for Bessel beam interaction with sapphire highlight that transport can significantly affect the plasma profile throughout extremely localized interactions inducing nanoplasmas.

II. THE TWO-FLUID PLASMA MODEL

The fluid model developed in this article is intended for materials that can be described by an isotropic parabolic band structure: the effective masses of conduction electrons and valence holes are independent of the direction and position in the Brillouin zone. The fluid model can be derived consistently by calculating moments of the kinetic equation with respect to velocity [34] and by assuming a local thermodynamic equilibrium [35] for electrons and holes. This implies Maxwellian distributions for both particle species. The fluid description allows us to save computational effort in comparison with the kinetic approach [36]. In our case, we consider that the plasma is sufficiently collisional to keep the particle distribution close to a Maxwellian distribution. The equations of the two-fluid plasma model in the balance law form (i.e., a conservative form on the left side of fluid equations and a source term on the right one) are given by [37,38]:

$$\frac{\partial}{\partial t}\begin{bmatrix} n_\mathrm{e} \\ n_\mathrm{e}\mathbf{u}_\mathrm{e} \\ \epsilon_\mathrm{e} \\ n_\mathrm{h} \\ n_\mathrm{h}\mathbf{u}_\mathrm{h} \\ \epsilon_\mathrm{h} \end{bmatrix} + \boldsymbol{\nabla}\cdot\begin{bmatrix} n_\mathrm{e}\mathbf{u}_\mathrm{e} \\ n_\mathrm{e}\mathbf{u}_\mathrm{e}\otimes\mathbf{u}_\mathrm{e} + \frac{p_\mathrm{e}}{m_\mathrm{e}^*}\mathbf{I} \\ (\epsilon_\mathrm{e}+p_\mathrm{e})\mathbf{u}_\mathrm{e} \\ n_\mathrm{h}\mathbf{u}_\mathrm{h} \\ n_\mathrm{h}\mathbf{u}_\mathrm{h}\otimes\mathbf{u}_\mathrm{h} + \frac{p_\mathrm{h}}{m_\mathrm{h}^*}\mathbf{I} \\ (\epsilon_\mathrm{h}+p_\mathrm{h})\mathbf{u}_\mathrm{h} \end{bmatrix} = \begin{bmatrix} 0 \\ \frac{n_\mathrm{e}q_\mathrm{e}}{m_\mathrm{e}^*}(\mathbf{E}+\mathbf{u}_\mathrm{e}\times\mathbf{B}) \\ n_\mathrm{e}q_\mathrm{e}\mathbf{u}_\mathrm{e}\cdot\mathbf{E} \\ 0 \\ \frac{n_\mathrm{h}q_\mathrm{h}}{m_\mathrm{h}^*}(\mathbf{E}+\mathbf{u}_\mathrm{h}\times\mathbf{B}) \\ n_\mathrm{h}q_\mathrm{h}\mathbf{u}_\mathrm{h}\cdot\mathbf{E} \end{bmatrix} + \begin{bmatrix} \mathbf{S}_\mathrm{e}^\mathrm{Coll} \\ \mathbf{S}_\mathrm{h}^\mathrm{Coll} \end{bmatrix}. \tag{1}$$

The system of equations (1) corresponds to three conservation laws for each fluid (electrons and holes): conservation of particle number, momentum, and energy. The term with the divergence operator is called the transport term, whereas the terms on the right are called the source terms. For a specie of particles a ($a = \mathrm{e}$ for conduction electrons and $a = \mathrm{h}$ for valence holes), q_a is the electric charge, m_a^* is the effective mass, n_a is the density, $\mathbf{u}_\mathrm{a}$ is the mean velocity, p_a is the scalar pressure, ϵ_a is the fluid energy density, $\mathbf{E}$ is the electric field, and $\mathbf{B}$ is the magnetic field. $\mathbf{I}$ is the identity matrix, and $\otimes$ is the tensor product. To obtain the system of equations (1), we additionally made the assumption that electron and hole fluids are nonviscous. The effects of viscosity are usually unimportant in ultrafast dynamics [39]. This allows us to consider scalar pressures instead of pressure tensors.

The system of equations for electron and hole fluids is closed by assuming local thermodynamic equilibrium (Maxwellian distribution) for both species:

$$\epsilon_\mathrm{a} \equiv \frac{p_\mathrm{a}}{\gamma-1} + \frac{1}{2}n_\mathrm{a}m_\mathrm{a}^*{\mathbf{u}_\mathrm{a}}^2, \tag{2}$$

where γ is the adiabatic index. The local thermodynamic equilibrium allows linking pressure and temperature through the ideal gas law [35]: $p_\mathrm{a} = n_\mathrm{a}k_\mathrm{B}T_\mathrm{a}$, where T_a is the temperature and k_B is the Boltzmann constant.

The terms $\mathbf{S}_\mathrm{e}^\mathrm{Coll}$ and $\mathbf{S}_\mathrm{h}^\mathrm{Coll}$ are the collisional terms for electron and hole fluids. We use the same general method as in Refs. [40,41] in order to include different physical phenomena; that is, we split the collisional terms in Eq. (1) into several terms:

$$\underbrace{\begin{bmatrix} \mathbf{S}_\mathrm{e}^\mathrm{Coll} \\ \mathbf{S}_\mathrm{h}^\mathrm{Coll} \end{bmatrix}}_{\equiv\mathbf{S}^\mathrm{Coll}} \equiv \underbrace{\begin{bmatrix} \mathbf{S}_\mathrm{e}^{\mathrm{e}-\mathrm{h}} \\ \mathbf{S}_\mathrm{h}^{\mathrm{e}-\mathrm{h}} \end{bmatrix}}_{\equiv\mathbf{S}^{\mathrm{e}-\mathrm{h}}} + \underbrace{\begin{bmatrix} \mathbf{S}_\mathrm{e}^{\mathrm{Imp}-\mathrm{e}} \\ \mathbf{S}_\mathrm{h}^{\mathrm{Imp}-\mathrm{e}} \end{bmatrix}}_{\equiv\mathbf{S}^{\mathrm{Imp}-\mathrm{e}}} + \underbrace{\begin{bmatrix} \mathbf{S}_\mathrm{e}^{\mathrm{Imp}-\mathrm{h}} \\ \mathbf{S}_\mathrm{h}^{\mathrm{Imp}-\mathrm{h}} \end{bmatrix}}_{\equiv\mathbf{S}^{\mathrm{Imp}-\mathrm{h}}} + \underbrace{\begin{bmatrix} \mathbf{S}_\mathrm{e}^{\mathrm{Ph}} \\ \mathbf{S}_\mathrm{h}^{\mathrm{Ph}} \end{bmatrix}}_{\equiv\mathbf{S}^{\mathrm{Ph}}} + \underbrace{\begin{bmatrix} \mathbf{S}_\mathrm{e}^{\mathrm{e}-\mathrm{p}} \\ \mathbf{S}_\mathrm{h}^{\mathrm{e}-\mathrm{p}} \end{bmatrix}}_{\equiv\mathbf{S}^{\mathrm{e}-\mathrm{p}}} + \underbrace{\begin{bmatrix} \mathbf{S}_\mathrm{e}^{\mathrm{h}-\mathrm{p}} \\ \mathbf{S}_\mathrm{h}^{\mathrm{h}-\mathrm{p}} \end{bmatrix}}_{\equiv\mathbf{S}^{\mathrm{h}-\mathrm{p}}}, \tag{3}$$

where the superscript e-h is related to electron-hole scattering, e-p is related to interactions between electrons and phonons, h-p is related to interactions between holes and phonons, Ph is related to photoionization, Imp-e is related to electron-initiated impact ionization, and Imp-h is related to hole-initiated impact ionization.

The electric and magnetic fields in Eq. (1) are determined by Maxwell equations:

$$\nabla \cdot \varepsilon_r \mathbf{E} = \frac{1}{\varepsilon_0}[q_e n_e + q_h n_h], \tag{4}$$

$$\nabla \cdot \mathbf{B} = 0, \tag{5}$$

$$\nabla \times \mathbf{E} = -\frac{\partial \mathbf{B}}{\partial t}, \tag{6}$$

$$\nabla \times \mathbf{B} = \mu_0 \mathbf{J} + \frac{1}{c^2}\frac{\partial \varepsilon_r \mathbf{E}}{\partial t}, \tag{7}$$

where ε_0 and μ_0 are, respectively, the vacuum permittivity and permeability. $c = (\varepsilon_0 \mu_0)^{-1/2}$ is the speed of light. ε_r is the relative permittivity of the background dielectric. The total current density $\mathbf{J}$ is composed of the contribution from conduction electrons and the one from valence holes:

$$\mathbf{J} = q_e n_e \mathbf{u}_e + q_h n_h \mathbf{u}_h. \tag{8}$$

In our description, we consider an electron-hole plasma localized in the background dielectric of relative permittivity ε_r. The effect of bound charges is also taken into account through relative permittivity ε_r, whereas the effect of charge carriers is included through the current density $\mathbf{J}$ in Eq. (8).

We finally remark that, here, the medium response to an electromagnetic excitation is taken into account through a fluid approach. This approach is valid only when the spatial scales are larger than the Debye length [42]. The typical densities involved in numerical results in Sec. IV are around 10^{21} cm^{-3}, and the temperatures are in the range of 1–100 eV, leading to a Debye length between 0.2 and 2 nm.

III. COLLISIONAL SOURCE TERMS

In this section, we specify the source terms $\mathbf{S}_e^{\mathrm{Coll}}$ and $\mathbf{S}_h^{\mathrm{Coll}}$ in Eq. (3). We include the different physical phenomena one by one in our model.

A. Electron-hole scattering

We start with the elastic scattering between conduction electrons and valence holes. We have chosen to include this phenomenon via the Bhatnagar-Gross-Krook (BGK) approach [43]. This approach assumes that the elastic scattering restores local equilibrium with an exponential decay in time. This description usually gives a first approximation to the problem under consideration [35] and is relatively easy to link to the Drude model of plasmas [44]. The inclusion of the BGK term in the two-fluid plasma equations is performed via the following source term [45]:

$$\mathbf{S}^{\mathbf{e-h}} = \begin{bmatrix} \mathbf{S}_e^{\mathbf{e-h}} \\ \mathbf{S}_h^{\mathbf{e-h}} \end{bmatrix} = \begin{bmatrix} 0 \\ -n_e \nu_{eh} \frac{\mu}{m_e^*}(\mathbf{u}_e - \mathbf{u}_h) \\ -\frac{\kappa \nu_{eh} n_e}{\gamma - 1}(T_e - T_h) + \frac{\kappa \nu_{eh} n_e}{2}\left[m_e^* \mathbf{u}_e{}^2 - m_h^* \mathbf{u}_h{}^2 + (m_h^* - m_e^*)\mathbf{u}_e \cdot \mathbf{u}_h\right] \\ 0 \\ -n_h \nu_{he} \frac{\mu}{m_h^*}(\mathbf{u}_h - \mathbf{u}_e) \\ -\frac{\kappa \nu_{he} n_h}{\gamma - 1}(T_h - T_e) + \frac{\kappa \nu_{he} n_h}{2}\left[m_h^* \mathbf{u}_h{}^2 - m_e^* \mathbf{u}_e{}^2 + (m_e^* - m_h^*)\mathbf{u}_h \cdot \mathbf{u}_e\right] \end{bmatrix}, \tag{9}$$

where $\mu = \frac{m_e^* m_h^*}{m_e^* + m_h^*}$ is the reduced mass, $\kappa = \frac{2\mu}{m_e^* + m_h^*}$, and ν_{eh} is the scattering frequency for momentum transfer from electrons to holes, whereas ν_{he} is from holes to electrons. Equation (9) is symmetrical to the permutation $e \leftrightarrow h$, and conservation of momentum and energy imposes the following condition [45]:

$$n_e \nu_{eh} = n_h \nu_{he}. \tag{10}$$

B. Interactions between charge carriers and phonons

As in Ref. [41], we consider two scattering phenomena for the interactions between charge carriers and phonons. The first one is the charge carrier–phonon elastic scattering, where charge carriers undergo a momentum change due to phonon emission/absorption. The second phenomenon is the carrier-phonon-photon interaction. In these two phenomena, the loss of energy to the phonon bath is negligible at the subpicosecond timescale [9,33]. The impact of these scattering events on the conduction electron fluid and on the valence hole fluid is a modification of the distribution of the particle, i.e., a reduction of the mean velocity and an increase of the thermal energy. We include these phenomena in a classical way (i.e., in a nonquantum treatment) via frictions terms [23]:

$$\mathbf{S}^{\mathbf{e-p}} = \begin{bmatrix} \mathbf{S}_e^{\mathbf{e-p}} \\ \mathbf{S}_h^{\mathbf{e-p}} \end{bmatrix} \equiv \begin{bmatrix} 0 \\ -n_e(\nu_{epp} + \nu_{ep})\mathbf{u}_e \\ 0 \\ 0 \\ \mathbf{0} \\ 0 \end{bmatrix}, \tag{11}$$

where ν_{epp} is the electron-phonon-photon interaction rate and ν_{ep} is the electron-phonon scattering rate. Similarly, we have for the hole fluid

$$\mathbf{S}^{\mathbf{h-p}} = \begin{bmatrix} \mathbf{S}_e^{\mathbf{h-p}} \\ \mathbf{S}_h^{\mathbf{h-p}} \end{bmatrix} \equiv \begin{bmatrix} 0 \\ \mathbf{0} \\ 0 \\ 0 \\ -n_h(\nu_{hpp} + \nu_{hp})\mathbf{u}_h \\ 0 \end{bmatrix}, \tag{12}$$

where ν_{hpp} is the hole-phonon-photon interaction rate and ν_{hp} is the hole-phonon scattering rate.

In this description with friction terms, the total energies ϵ_a of the fluids do not change [no term in the third and sixth components of Eqs. (11) and (12)]. The scattering induces a conversion of directed energy $\frac{1}{2} n_a m_a^* \mathbf{u}_a{}^2$ into thermal energy

$\frac{p_a}{\gamma-1}$. It also induces a weakening of the current density $\mathbf{J}$, thus absorbing energy from the electromagnetic fields.

We note that here, we discard the energy transfer from the carriers to the phonon bath since it is effective at timescales of several picoseconds, while our model is intended to model typically subpicosecond dynamics [9,33].

C. Electron-electron and hole-hole scattering

Electron-electron and hole-hole elastic scattering do not affect fluid equations (1) [29,35]. The reason is that in the fluid approach, the shape of the distribution is fixed to a Maxwellian one, before and after the scattering process. In addition, during a scattering event, the change in momentum (energy) of a particle is equal to the change in momentum (energy) of the other particle. This implies that the total momentum (energy) of the fluid remains constant during elastic scattering between particles of the same species [35].

D. Photoionization

Photoionization, impact ionization, and recombination can be considered inelastic collisions [35]. However, it is conventionally difficult to rigorously describe inelastic collisions in the framework of the fluid description [46]. In this section, we insert photoionization (promotion of electrons in the conduction band by absorption of field energy) into the two-fluid plasma model. Impact ionization will be modeled in the following section. We start by defining n_{ev} as the density of electron available in the valence band: this number is a function of time and space. We set n_0 as the initial density of electrons available in the valence band and α^{Ph} as the photoionization rate (in $m^{-3}\ s^{-1}$).

To include photoionization, we make the following assumptions: (i) The number of created fluid particles (electrons and holes) through photoionization is given by the rate equation used in Ref. [17] ($\frac{\partial}{\partial t} n_e = \frac{n_{ev}}{n_0}\alpha^{Ph}$). We use the Keldysh ionization rate in solids [47] (see the Appendix), but it could be replaced by more sophisticated models [48] without changing the overall architecture of our model. (ii) As in Ref. [49], we consider that during photoionization, valence electrons are promoted to the bottom of the conduction band. This is equivalent to neglecting the residual energy transfer to charge carriers after photoionization: fluid particles are generated with zero energy ($p_a = 0$ and $\mathbf{u}_a = \mathbf{0}$).

The source term for photoionization of Eq. (3) is therefore given by

$$\mathbf{S}^{\mathbf{Ph}} \equiv \begin{bmatrix} \mathbf{S}_e^{\mathbf{Ph}} \\ \mathbf{S}_h^{\mathbf{Ph}} \end{bmatrix} \equiv \begin{bmatrix} \frac{n_{ev}}{n_0}\alpha^{Ph} \\ \mathbf{0} \\ 0 \\ \frac{n_{ev}}{n_0}\alpha^{Ph} \\ \mathbf{0} \\ 0 \end{bmatrix}. \tag{13}$$

For each electron-hole pair generated, one valence electron must be removed. This leads to the following rate equation for the density of valence electrons:

$$\frac{\partial}{\partial t} n_{ev} = -\frac{n_{ev}}{n_0}\alpha^{Ph}. \tag{14}$$

Moreover, to ensure energy conservation, we have to remove the ionization energy from the electromagnetic fields. We use a fictive ionization current density as in Refs. [39,50]:

$$\mathbf{J}^{Ph} = \frac{n_{ev}}{n_0}\frac{\alpha^{Ph} U_g}{\mathbf{E}^2}\mathbf{E}, \tag{15}$$

where U_g is the dielectric band gap. The fictive ionization current density (15) is added to the current density in the Maxwell-Ampère equation (7).

E. Impact ionization

In this section, we include impact ionization in the two-fluid plasma model. We consider electron-initiated impact ionization and hole-initiated impact ionization. In the first phenomenon, an above-threshold energetic conduction electron collides with a valence electron: the valence electron is promoted to the conduction band, and a hole is left in the valence band. A symmetric scenario can happen in the valence band with an energetic hole.

To include electron-initiated impact ionization in the two-fluid plasma model, we define α^e, the reaction rate (in s^{-1}). We model the number of created fluid particles (electrons and holes) through impact ionization via a rate equation used in Ref. [17], $\frac{\partial}{\partial t} n_e = \frac{n_{ev}}{n_0}\alpha^e n_e$. As in the case of photoionization, we consider that fluid particles are generated with zero energy ($p_a = 0$ and $\mathbf{u}_a = \mathbf{0}$).

The source term for electron-initiated impact ionization becomes

$$\mathbf{S}^{\mathbf{Imp-e}} \equiv \begin{bmatrix} \mathbf{S}_e^{\mathbf{Imp-e}} \\ \mathbf{S}_h^{\mathbf{Imp-e}} \end{bmatrix} \equiv \begin{bmatrix} \frac{n_{ev}}{n_0}\alpha^e n_e \\ \mathbf{0} \\ -\frac{n_{ev}}{n_0} n_e \alpha^e U_g \\ \frac{n_{ev}}{n_0}\alpha^e n_e \\ \mathbf{0} \\ 0 \end{bmatrix}. \tag{16}$$

For hole-initiated impact ionization, these equations are

$$\mathbf{S}^{\mathbf{Imp-h}} \equiv \begin{bmatrix} \mathbf{S}_e^{\mathbf{Imp-h}} \\ \mathbf{S}_h^{\mathbf{Imp-h}} \end{bmatrix} \equiv \begin{bmatrix} \frac{n_{ev}}{n_0}\alpha^h n_h \\ \mathbf{0} \\ 0 \\ \frac{n_{ev}}{n_0}\alpha^h n_h \\ \mathbf{0} \\ -\frac{n_{ev}}{n_0} n_h \alpha^h U_g \end{bmatrix}, \tag{17}$$

and the corresponding rate equation for the density of valence electrons reads

$$\frac{\partial}{\partial t} n_{ev} = -\frac{n_{ev}}{n_0}\alpha^e n_e - \frac{n_{ev}}{n_0}\alpha^h n_h. \tag{18}$$

Impact ionization rates are usually calculated from Fermi's golden rule and depend on particle energy. The Keldysh impact ionization rate for a single particle is given by [49,51]

$$\alpha^{Single} = \begin{cases} \alpha_0^e \left(\frac{E_e - E_T}{U_g}\right)^{\Upsilon} & \text{for } E_e \geqslant E_T, \\ 0 & \text{for } E_e < E_T, \end{cases} \tag{19}$$

where E_e is the energy of the initiator electron, the exponent is $\Upsilon = 2$ [51], and E_T is the threshold energy of the reaction:

$$E_T = \frac{1 + 2\frac{m_e^*}{m_h^*}}{1 + \frac{m_e^*}{m_h^*}} U_g. \tag{20}$$

The coefficient α_0^e is given by [51]

$$\alpha_0^e = \left(\frac{q_e^2}{4\pi\epsilon_0}\right)^2 \frac{m_e^* A_c^2 A_v^2}{\varepsilon_r^2 \hbar^3 \left(1 + 2\frac{m_e^*}{m_h^*}\right)^{3/2}}, \tag{21}$$

where A_c and A_v are overlapping integrals between the initial states and final states of the conduction electron and valence electron involved in the reaction [51].

In order to extend the rate α^{Single} for a single particle to fluid particles, Peñano *et al.* [49] used the energy distribution of particles to determine an effective impact ionization rate in the fluid description based on a centered Maxwellian velocity distribution ($\mathbf{u}_a = \mathbf{0}$). In a strong laser field, the mean velocity of particles can be important: we therefore generalized this approach to a noncentered Maxwellian velocity distribution. The velocity distribution for particles of species a is given by\vskip-2pt

$$\begin{aligned} G_a(E_a) = {} & \frac{2}{\sqrt{\pi} m_a^* ||\mathbf{u}_a||} \left[\frac{m_a^*}{2k_B T_a}\right]^{1/2} \\ & \times \exp\left(-\frac{m_a^*}{2k_B T_a}\left[\frac{2E_a}{m_a^*} + ||\mathbf{u}_a||^2\right]\right) \\ & \times \sinh\left(\frac{m_a^* ||\mathbf{u}_a||}{k_B T_a}\sqrt{\frac{2E_a}{m_a^*}}\right). \end{aligned} \tag{22}$$

For $\mathbf{u}_a = \mathbf{0}$, Eq. (22) gives the formula given in Peñano *et al.* [49]. The effective impact ionization rate in the fluid description is obtained by integrating the impact ionization rate for a single particle α^{Single} over the energy distribution $G_a(E_a)$:

$$\alpha^a = \int_0^\infty \alpha^{\text{Single}}(E_a) G_a(E_a) dE_a. \tag{23}$$

For reference, we plot in Fig. 1 the result of numerical integration of Eq. (23) as a function of $k_B T_a$ in α-phase sapphire for two different mean velocities (blue line for $||\mathbf{u}_a|| = 0$ and dashed red line for the typical mean velocity encountered in the simulations in Sec. IV, i.e., $||\mathbf{u}_a|| = 3\times10^6$ m/s).

F. Comments

The effective approach we use could be completed further by other mechanisms. For now, electron-hole-photon scattering is not done explicitly here since it would be modeled with a friction term similar to those in Eqs. (11) and (12).

We neglected Auger recombinations (inverse process of electron-initiated and hole-initiated impact ionizations) since the timescale of this phenomenon is typically picoseconds [9]. However, we remark that these phenomena can be included in the two-fluid plasma model in a way similar to that in Secs. III D and III E.

The generation of self-trapped excitons is a nonradiative recombination mechanism in which a conduction electron and a valence hole are bound via a Coulomb interaction in the vicinity of an impurity of the material [18]. This phenomenon can be important in subpicosecond dynamics of dielectrics such as fused silica [53]. In the following, we will consider dielectrics in which this phenomenon is negligible (sapphire or magnesium oxide [54,55]), but self-trapped-exciton generation can be included in the two-fluid plasma model with the same reasoning as before.

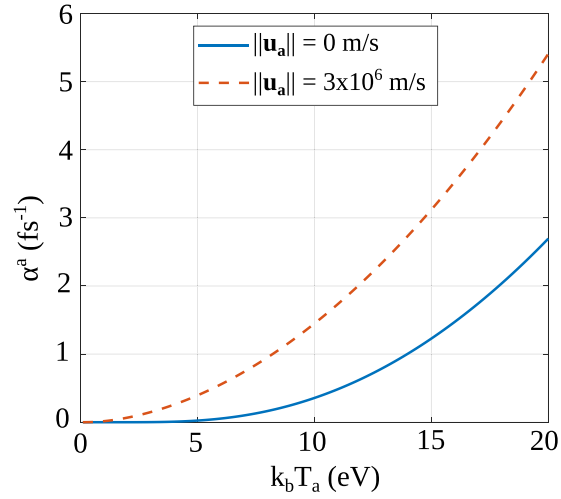

FIG. 1. Impact ionization rate in α-phase sapphire as a function of $k_B T_a$. We set $m_a^* = 0.4 m_e$ [25] and $U_g = 10$ eV [52].

IV. NUMERICAL SIMULATIONS OF FEMTOSECOND BESSEL PULSE EXCITATION OF DIELECTRICS

In this section, we use the model presented above to numerically investigate transport phenomena in the framework of femtosecond laser pulse excitation of transparent materials in a regime close to or above the ablation threshold. We show that the transport phenomena can strongly affect the plasma density profile in the case of localized laser-plasma interactions. In previous work, we developed a numerical scheme to integrate the two-fluid plasma system of equations combined with Maxwell equations. Here, we use the pseudospectral analytical time-domain method (PSATD) to solve Maxwell's curl equations and the Lax-Wendroff scheme to solve fluid equations [56]. This approach has the benefit of avoiding grid staggering in space and imposes fewer constraints on sampling than other techniques [44].

The physical situation we investigate corresponds typically to the case of plasma formation inside the bulk of α-phase sapphire by a highly focused femtosecond zeroth-order Bessel beam. We use parameters corresponding to a regime where laser-generated nanoplasmas were experimentally shown to open a void in the bulk [57].

A. Numerical setup

In our simulations, the beam is linearly polarized along the x direction while propagating along the z direction. We use the fact that the Bessel beam intensity profile is invariant along the propagation direction to model only a three-dimensional box with a length corresponding to one optical phase period in the z axis [58].

The size of the numerical box is $N_x = N_y = 460$, and $N_z = 26$. For the x and y directions, we use perfectly matched layers

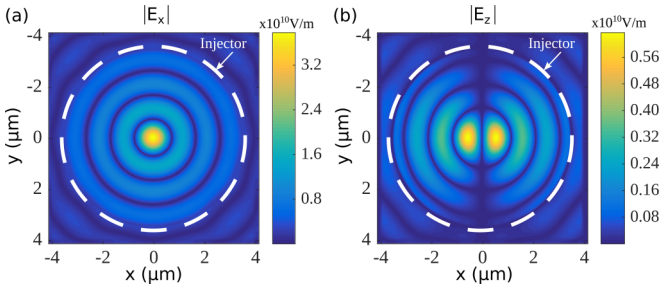

FIG. 2. (a) $|E_x|$ component at $t = 0$ fs for the x-polarized zeroth-order Bessel beam in the absence of plasma and ionization. (b) $|E_z|$ component at $t = 1.9$ fs (maximal value). The dashed white line corresponds to the position the injector.

for PSATD [59] and Neumann boundary conditions for the fluid solver, where the spatial derivatives of fluid variables are set to zero. Furthermore, we use periodic boundary conditions in the z direction for both solvers. The spatial step is $\Delta x = \Delta y = \Delta z \approx 18.0$ nm, whereas the temporal step is $\Delta t \approx 53.3$ as (with the PSATD algorithm, the Courant condition is not necessary [44]).

The zeroth-order Bessel beam is injected using the cylindrical antenna presented in Ref. [58]. The laser pulse has a Gaussian temporal profile of the full width at half maximum of 100 fs in intensity, with a cone angle in vacuum $\theta = 25^\circ$ (equivalent to $\theta_m = 13.9^\circ$ in sapphire). The wavelength in vacuum is $\lambda_0 = 0.8\,\mu$m. The transverse electric field distributions of components E_x and E_z around $t = 0$ fs (i.e., maximum of the temporal profile) are plotted in Fig. 2. The time is zero when the peak intensity of the pulse reaches the center and the simulation started at $t = -334$ fs. The peak amplitude of the electric field in Fig. 2, i.e., $E \simeq 3\times10^{10}$ V/m, corresponds to an intensity of 4×10^{14} W/cm^2 in $(x, y) = (0, 0)$. The maximum of the amplitude of the beam will vary in the next simulations, but the other parameters will remain the same. Furthermore, we remark that the component E_y of the electric field is negligible [58].

The relative permittivity of sapphire is $\varepsilon_r = 3.09$. We neglect the anisotropy of the dielectric in order to simplify the problem. The band gap is $U_g = 10$ eV [52]. In Secs. IV B and IV C, the effective mass of conduction electrons is $m_e^* = 0.4m_e$ [25], and the effective mass of valence holes is $m_h^* = 0.4m_e$ [25]. In contrast, in Sec. IV D, we explore the impact of the variation of the effective mass ratio. The initial density of electrons available in the last valence band is $n_0 = 2.35\times10^{22}$ cm^{-3} [60].

B. Transport following resonance absorption

Reference [61] demonstrates the importance of resonance absorption in the energy deposition process within dielectrics when highly focused femtosecond Bessel beams are used. In that reference, the simulations were performed for an electron/ion plasma, i.e., assuming that either the holes are heavy or the induced plasma is sufficiently dense to erase the band structure, which can happen when, typically, 5%–10% of the valence electrons are promoted to the conduction band [62,63]. Here, in contrast, we assume that the band structure remains, and we study resonance absorption with light holes.

We start here with the simulation of interaction between a preexisting electron-hole plasma inside sapphire with a femtosecond Bessel pulse in the absence of ionization in order to isolate the phenomenon of plasma wave excitation through resonance absorption. We use the pulse parameters described in the previous section, except that we reduce the peak intensity to $I_{Max} = 4\times10^{12}$ W/cm^2 in order to show that transport of the electron-hole plasma can already have an important impact at relatively low intensities. We use the same order of magnitudes of the plasma parameters as in Ref. [22]. The initial density profile (in cm^{-3}) is defined by

$$n_e(t=0) = \begin{cases} 0 & r > R_0, \\ 1.5\times10^{21}\cos^2\left(\frac{\pi r}{2R_0}\right) & r \leqslant R_0, \end{cases} \tag{24}$$

with $r = \sqrt{x^2 + y^2}$ and $R_0 = 540$ nm. This profile is initially invariant in the z direction, and the plasma is initially neutral: $n_e = n_h$. A crosscut of the initial density profile is shown in Fig. 3(a).

We set the scattering rates with phonons as $\nu_e = \nu_{epp} + \nu_{ep} = 0.05$ fs^{-1}, $\nu_h = \nu_{hpp} + \nu_{hp} = 0.05$ fs^{-1}, following the order of magnitude provided by Ref. [11]. We neglect electron-hole scattering ($\nu_{eh} = 0$ fs^{-1}) in order to isolate and to observe clearly the excited plasma waves, which are otherwise partly damped.

Before discussing the numerical results, we define the critical density, which is the density at which the real part of the total permittivity is zero:

$$n_c = \frac{\varepsilon_r\varepsilon_0\omega_0^2}{q_e^2}\left[\frac{1}{m_e^*\left(1+\frac{\nu_e^2}{\omega_0^2}\right)} + \frac{1}{m_h^*\left(1+\frac{\nu_h^2}{\omega_0^2}\right)}\right]^{-1} = 1.08\times10^{21}\ \text{cm}^{-3}. \tag{25}$$

We note this value highly depends on the effective masses of electrons and holes. The critical density is shown with a yellow circle in Fig. 3(a). We also define the density at the turning point (density at which total reflection occurs for the incidence angle $\pi/2 - \theta_m$ of the Bessel beam on the plasma inside the medium) [64]:

$$n_t = n_c \sin^2\theta_m = 0.06\times10^{21}\ \text{cm}^{-3}. \tag{26}$$

Figure 3 summarizes our results. In Fig. 3(b), the distribution of the x component of the electric field is shown at a time slightly before the peak of the pulse. We observe that the central lobe of the Bessel beam cannot form because of the reflection at the turning point. This is apparent in the crosscut shown in Fig. 3(d). The evanescent field can still penetrate into the plasma up to the critical surface and excite the resonance. The resonance peaks are visible in the field cross section in Fig. 3(b) and correspond to the resonance absorption phenomenon (excitation of plasma waves by a p-polarized electromagnetic field) [64]. We observe in the distribution of pressure [Fig. 3(c)] the localized heating of the plasma at the resonance. The amplitude of the field due to the plasma waves reaches $\simeq 10^9$ V/m in an important temporal range ($-120 < t < 100$ fs). The resonance peaks therefore correspond to significant field gradients (variation of 10^9 V/m over 50 nm) and strong gradients of pressure (variation of 10^7 Pa over 50 nm). The pressure and ponderomotive forces

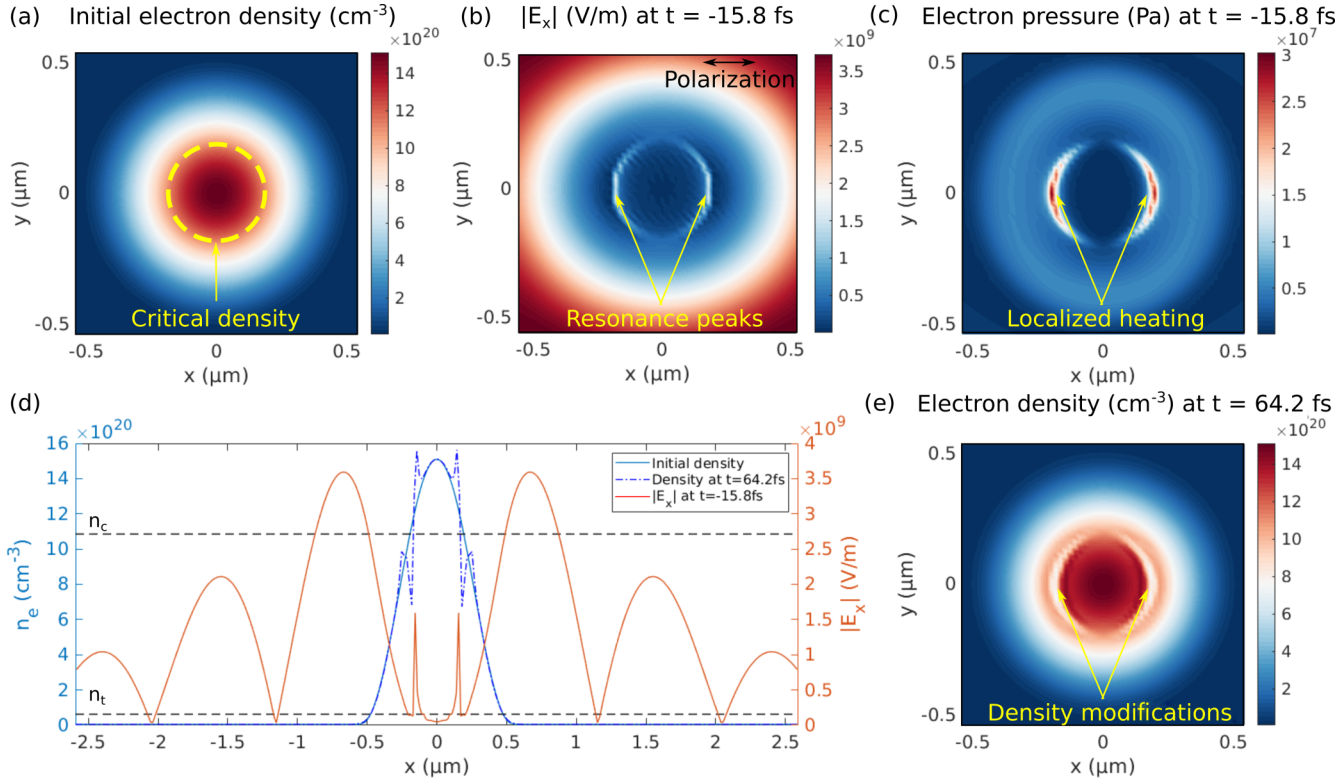

FIG. 3. (a) Initial electron density profile. (b) Numerical field at $t = -15.8$ fs. (c) Electron pressure at $t = -15.8$ fs. (d) x cuts of the plasma density distribution at the initial time (solid blue line) and at $t = 64.2$ fs (dot-dashed blue line) and numerical field at $t = -15.8$ fs (red line). Horizontal dashed black lines indicate the critical density and the density at the turning point. (e) Electron density profile at $t = 64.2$ fs.

lead to a sharp depletion of the plasma density around the critical surface, as can be seen in Figs. 3(d) and 3(e).

It is therefore important to take into account the transport terms in the modeling of electron-hole nanoplasmas with light holes even at very moderate intensity (10^{12} W/cm^2) since the excitation of plasma waves can affect the density profile and nonlinear ionization. Furthermore, we note that, when the effective mass of holes is comparable to the electron mass, the position of critical density can be strongly affected, which is apparent from Eq. (25), as well as the response of the medium to the field excitation.

The density profiles of electrons and holes are very close: the difference $(n_e - n_h)$ is typically around 10^{19} cm^{-3} (1%) and originates from the difference in trajectory under the electric field. This charge separation, over a distance of only $\Delta x = 18$ nm, is enough to create a Coulomb field of 10^9 V/m. The associated restoring force prevents more significant charge separation.

We finally highlight that our model, like most hydrodynamic models, cannot capture collisionless absorption by effects such as Landau damping [61] because the distributions are fixed to isotropic Maxwellian ones. This mechanism is partially responsible for the plasma wave absorption, and its modeling requires a kinetic approach (Vlasov equation) or particle description, e.g., particle-in-cell codes [64].

C. Simulations with ionization

In this section, we compare the influence of the transport terms in the presence of ionization. We use here a peak intensity of $I_{\mathrm{Max}} = 10^{14}$ W/cm^2. Regarding the impact ionization rates (electron initiated and hole initiated), we set at first approximation $A_c = A_v = 1$ for the overlapping integrals [51], and the exponent is $\Upsilon = 2$ [51]. The electron-hole scattering rate is calculated following Ref. [29] ($\nu_{eh} = \frac{\sqrt{3}\varepsilon_0\pi(k_B T_e)^{3/2}}{2q_e^2}\sqrt{\frac{1}{m_e^*}+\frac{1}{m_h^*}}$), and we reduce the rates of interaction with phonons ($\nu_{epp} + \nu_{ep}$ and $\nu_{hpp} + \nu_{hp}$) to $\nu = 0.01$ fs^{-1} [65] in order to observe the transport phenomenon clearly. We will comment on the relevance of these rates at the end of this section.

Figure 4 compares the (x, t) distributions of intensity, plasma density, and pressure for a simulation without the transport term in Eq. (1) (left panels) and for a simulation including this term (right panels). As in the previous section, the density profile of holes is quasi-indistinguishable from the electron one due to the Coulomb attraction, and it is not shown here.

Before $t < -50$ fs, both simulations exhibit similar behavior. We first observe in Figs. 4(a) and 4(d) the progressive buildup of the central lobe of the Bessel beam, with peak intensity reaching $I = 3.3\times10^{13}$ W/cm^2. Around $t = -50$ fs, the laser intensity is sufficiently high to generate charge density up to 2.5×10^{21} cm^{-3} through ionization processes [Figs. 4(b) and 4(e)]. The plasma is then sufficiently dense to deflect the beam because of the wave-turning phenomenon mentioned earlier, which prevents the formation of the central lobe on the optical axis. The resonance peaks discussed in the previous section are not clearly visible here for two reasons. First, the electron-hole scattering rate is stronger than in the

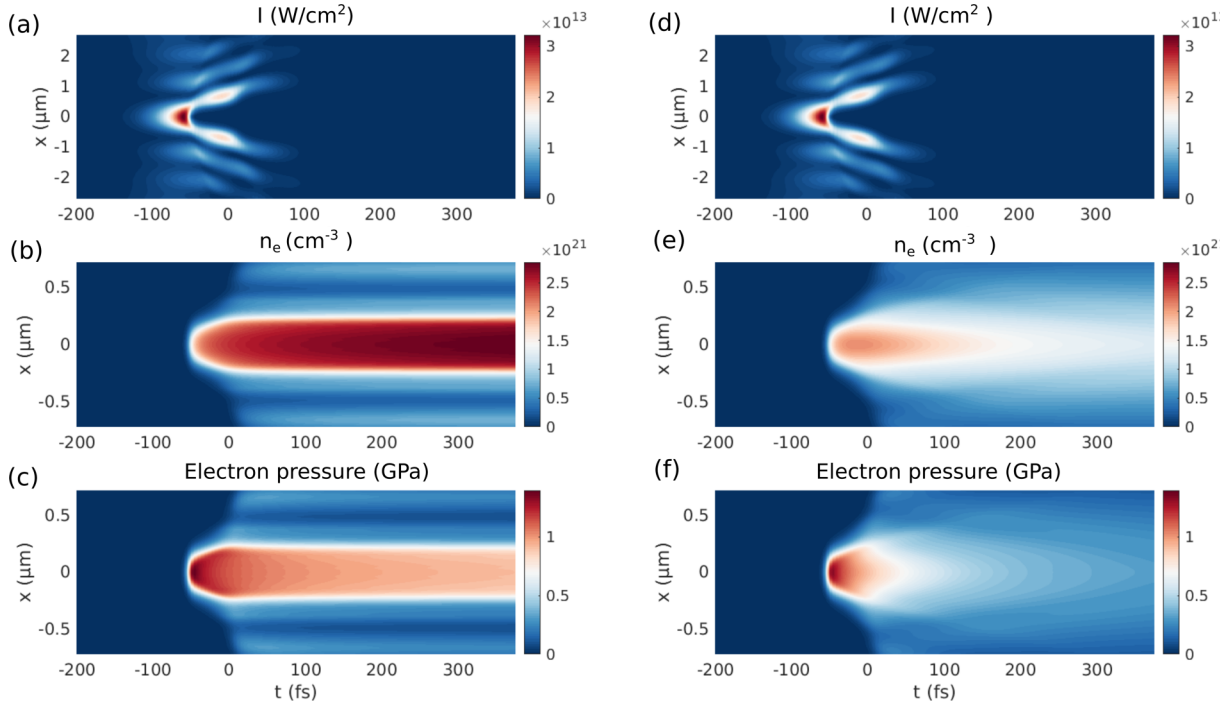

FIG. 4. (a) Intensity, (b) electron density, and (c) electron pressure from the simulation performed without integrating the transport term in Eq. (1). (d) Intensity, (e) electron density, and (f) electron pressure from the simulation including the transport term.

previous section: while it was set to zero in the previous section, it now varies in the range $\nu_{eh} = 0$–$3\ \mathrm{fs}^{-1}$. This implies that the energy of the plasma waves is quickly converted into thermal energy. Second, the distributions of density and temperature evolve in time: the position of the critical density shifts, which prevents an extremely localized excitation. We also remark that the intensity profiles show almost no difference since transport effects mainly occur when the laser pulse has left the numerical box.

We observe in both simulations that the electron pressures exceed 1 GPa at $t = -45$ fs [see Figs. 4(c) and 4(f)]. The pressure increase is due to the direct absorption of laser energy during the scattering processes undergone by charge carriers and is also due to the resonance absorption mentioned in the previous section. The strong variations of pressure ($\simeq$1 GPa) over a small spatial scale ($\simeq$100 nm) are responsible for the main differences in the dynamics between the two simulations after the pulse peak. In the simulation performed without the transport term [Fig. 4(b)], the on-axis density continues to increase because of the impact ionization process, and the critical density is exceeded, in agreement with simulations in Ref. [22] where the transport is neglected. Simultaneously, the pressure decreases since impact ionization reduces the temperature of the conduction band electrons.

In contrast, the simulation performed with transport integration shows a significant relaxation of the pressure and density profiles [see Figs. 4(e) and 4(f)]. The final maximum density (resp. pressure) is around 2 times (resp. 4 times) less than the one obtained in the simulation without transport integration but is still close to the critical density, in agreement with experimental results [61]. The transport induces the expansion of the electron-hole plasma and tends to weaken the impact ionization effects.

Furthermore, we remark that the rate of collisions with phonons influences the transport: when ν is increased, for instance, from 0.01 to 0.05 fs^{-1}, the transport effect is highly damped. We also remark that, in contrast, electron-hole scattering has a much lower impact on transport. Indeed, in the case where electrons and holes have similar masses, their mean velocities $\mathbf{u}_e$ and $\mathbf{u}_h$ are very close during the transport period. In Eq. (9), most terms related to momentum transfer involve the difference in these velocities, which implies the collisional source term becomes almost negligible even if ν_{eh} is relatively high.

The simulations done in this and the last section show the importance of transport effects induced by the strong gradients generated by tightly focused pulses. We observed at moderate intensities ($\simeq 10^{14}$ W/cm^2) and at a subpicosecond timescale transport over a few hundred nanometers, which is not negligible for plasmas with submicrometer dimensions.

D. The role of the effective mass

In this section, we show the plasma density buildup in situations with different effective masses of valence holes. We keep the effective mass of the conduction electrons to $m_e^* = 0.4m_e$ [25]. We plot in Figs. 5(a)–5(c) the electron density maps resulting from three different numerical simulations with different hole masses: (a) $m_h^* = 0.4m_e$ (the simulation in the previous section), (b) $m_h^* = 2m_e$, and (c) $m_h^* = 102\times1836m_e$ (corresponding to molecular mass in sapphire), respectively. We also plot, for the same three cases [Figs. 5(d)–5(f)], the temporal evolution of pressures and density of both species in $x = y = z = 0$ as a function of time.

In Fig. 5(a), we notice the significant transport already discussed in the previous section, inducing a spatial expansion of the plasma. In Fig. 5(b), we remark a significant reduction

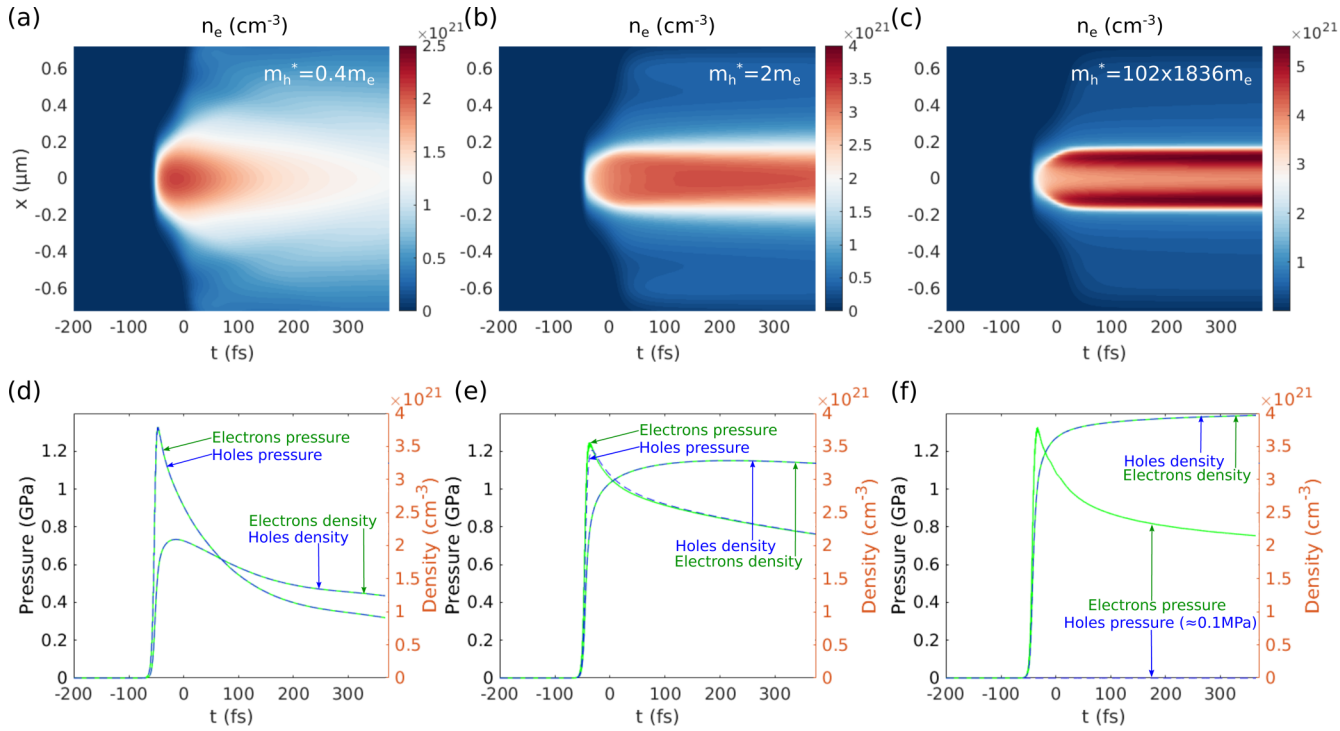

FIG. 5. $(x-t)$ distributions of electron densities for three different hole masses: (a) $m_h^* = 0.4m_e$, (b) $m_h^* = 2m_e$, and (c) $m_h^* = 102\times1836m_e$. Pressures and densities, at $x = y = z = 0$, of electrons (solid green lines) and holes (dashed blue lines) for the same three cases: (d) $m_h^* = 0.4m_e$, (e) $m_h^* = 2m_e$, and (f) $m_h^* = 102\times1836m_e$.

in the transport compared to Fig. 5(a). The plasma expansion is totally negligible in Fig. 5(c), as observed in the literature for materials with $m_h^* \gg m_e^*$ [21]. This transport reduction is explained by the Coulomb attraction discussed in Sec. IV B.

In this last case, the electron pressure peaks at around 1.2 GPa, but the hole pressure is much lower [0.1 MPa; Fig. 5(f)]. This corresponds to electron temperature around 2 eV and hole temperature around 0.1 meV [$T_a = p_a/(n_a k_B)$]. Since the mass ratio is around 10^6, the energy transfer from the warm electron fluid is not significant at the femtosecond timescale. Indeed, the timescale for the energy transfer from electrons to holes is related to the rate in Eq. (9) ($\frac{1}{\kappa\nu_{eh}} \approx \frac{m_h^*}{m_e^*}\frac{1}{\nu_{eh}} \approx 500$ ps). In Fig. 5(e), we remark at $t \approx -50$ fs that the hole pressure is slightly below the electron pressure since holes are slightly heavier than electrons. We also remark quick thermalization occurring for $-50 < t < 50$ fs, leading to a superimposition of the pressures curves for $t > 50$ fs.

Furthermore, we note in Figs. 5(d)–5(f) that the densities of holes and electrons are superimposed due to the Coulomb force, as discussed in Sec. IV B.

The hole mass also impacts the plasma buildup. Although the transport is weak in both simulations in Figs. 5(b) and 5(c), they exhibit different density profiles. The reason is that the mass ratio significantly affects the cutoff frequency, the field ionization, and impact ionization rates.

V. CONCLUSION

We developed a theoretical approach based on the two-fluid plasma model in order to describe extremely localized interaction (<1 μm) of ultrashort laser pulses within solids. This model is well suited to describe transport effects, plasma waves effects, and the dynamics of conduction electrons and valence holes, as well as electron-hole scattering, photoionization, impact ionization, and interactions between carriers and phonons. Numerical results based on this model showed the significance of these effects in laser-induced nanoplasmas within dielectrics where valence holes are light. This model can be refined in future works by including additional effects such as the Kerr effect or the Raman effect. We also believe that transport phenomena can shed new light on the ultrafast dynamics of the thin layers of laser-produced electron-hole plasmas at the surface of dielectrics, which allow measurements of a number of transition cross sections [18,66,67]. We anticipate that this approach will open new perspectives in the understanding of the interaction of ultrashort laser pulses with dielectrics and semiconductors.

ACKNOWLEDGMENTS

The research leading to these results has received funding from the European Research Council (ERC) under the European Union's Horizon 2020 research and innovation program (Grant Agreement No. 682032-PULSAR), Région Bourgogne Franche-Comté, Labex ACTION ANR-11-LABX-0001-01, the I-SITE BFC project (Contract No. ANR-15-IDEX-0003), and the EIPHI Graduate School (Contract No. ANR-17-EURE-0002). We acknowledge the support of Mésocentre de Calcul de Franche-Comté.

APPENDIX: KELDYSH PHOTOIONIZATION RATE

For completeness, we provide the expression for the Keldysh photoionization rate in solids used here (in s^{-1} m^{-3}) [11,47]:

$$\alpha^{\mathrm{Ph}} = \frac{2\omega_0}{9\pi}\left(\frac{\omega_0\mu}{\hbar\gamma_1}\right)^{3/2} Q(\Gamma, x) \times \exp\left[-\pi \mathsf{E}(x+1)\frac{K(\gamma_1^2) - G(\gamma_1^2)}{G(\gamma_2^2)}\right]. \quad \text{(A1)}$$

The symbol $\mathsf{E}(x)$ represents the integer part of the number x, $\hbar$ is the reduced Planck constant, $\mu = \frac{m_e^* m_h^*}{m_e^* + m_h^*}$, $\Gamma = \omega_0\sqrt{\mu U_g}/|q_e|||\mathbf{E}||$ is the Keldysh parameter, and $||\mathbf{E}||$ is the amplitude of laser field. Functions K and G are elliptical integrals of the first and second kind, $\gamma_1 = \Gamma/\sqrt{1+\Gamma^2}$, and $\gamma_2 = \gamma_1/\Gamma$. The function $Q(\Gamma, x)$ of Eq. (A1) is given by [47]

$$Q(\Gamma, x) = \sqrt{\frac{\pi}{2K(\gamma_2^2)}} \sum_{n=0}^{\infty} \exp\left[-\pi n \frac{K(\gamma_1^2) - G(\gamma_1^2)}{G(\gamma_2^2)}\right] \times \Phi\left(\frac{\pi}{2}\sqrt{\frac{2\mathsf{E}(x+1) - 2x + n}{K(\gamma_2^2)G(\gamma_2^2)}}\right), \quad \text{(A2)}$$

where $\Phi(z) = \int_0^z \exp(y^2 - z^2)dy$ and $x = \tilde{U}/\hbar\omega_0$. $\tilde{U}$ is the effective band gap of the material, given by

$$\tilde{U} = \frac{2U_g}{\pi\gamma_1} G(\gamma_2^2). \quad \text{(A3)}$$

We remark that the effective masses of electrons and holes highly influence the photoionization rate. They can increase by almost two orders of magnitude when the hole mass is modified from $m_h^* = 7.5m_e$ (heavy holes in sapphire [25]) to $m_h^* = 0.4m_e$ (light holes in sapphire [25]).

[1] R. Gattass and E. Mazur, Femtosecond laser micromachining in transparent materials, Nat. Photon. **2**, 219 (2008).

[2] K. Sugioka and Y. Cheng, Ultrafast lasers-reliable tools for advanced materials processing, Light Sci. Appl. **3**, e149 (2014).

[3] N. M. Bulgakova, V. P. Zhukov, Y. P. Meshcheryakov, L. Gemini, J. Brajer, D. Rostohar, and T. Mocek, Pulsed laser modification of transparent dielectrics: What can be foreseen and predicted by numerical simulations?, J. Opt. Soc. Am. B **31**, C8 (2014).

[4] M. Malinauskas, A. Žukauskas, S. Hasegawa, Y. Hayasaki, V. Mizeikis, R. Buividas, and S. Juodkazis, Ultrafast laser processing of materials: From science to industry, Light: Sci. Appl. **5**, e16133 (2016).

[5] A. Vogel, J. Noack, G. Hüttman, and G. Paltauf, Mechanisms of femtosecond laser nanosurgery of cells and tissues, Appl. Phys. B **81**, 1015 (2005).

[6] M. Noorhafiza and L. Lin, Underwater femtosecond laser micromachining of thin nitinol tubes for medical coronary stent manufacture, Appl. Phys. A **107**, 849 (2012).

[7] R. Meyer, L. Froehly, R. Giust, J. Del Hoyo, L. Furfaro, C. Billet, and F. Courvoisier, Extremely high-aspect-ratio ultrafast Bessel beam generation and stealth dicing of multi-millimeter thick glass, Appl. Phys. Lett. **114**, 201105 (2019).

[8] I. Mirza, N. M. Bulgakova, J. Tomastik, V. Michàlek, O. Haderka, L. Fekete, and T. Mocek, Ultrashort pulse laser ablation of dielectrics: Thresholds, mechanisms, role of breakdown, Sci. Rep. **6**, 39133 (2016).

[9] S. K. Sundaram and E. Mazur, Inducing and probing non-thermal transitions in semiconductors using femtosecond laser pulses, Nat. Mater. **1**, 217 (2002).

[10] P. Jürgens, M. J. J. Vrakking, A. Husakou, R. Stoian, and A. Mermillod-Blondin, Plasma formation and relaxation dynamics in fused silica driven by femtosecond short-wavelength infrared laser pulses, Appl. Phys. Lett. **115**, 191903 (2019).

[11] L. Sudrie, A. Couairon, M. Franco, B. Lamouroux, B. Prade, S. Tzortzakis, and A. Mysyrowicz, Femtosecond Laser-Induced Damage and Filamentary Propagation in Fused Silica, Phys. Rev. Lett. **89**, 186601 (2002).

[12] A. Couairon, L. Sudrie, M. Franco, B. Prade, and A. Mysyrowicz, Filamentation and damage in fused silica induced by tightly focused femtosecond laser pulses, Phys. Rev. B **71**, 125435 (2005).

[13] M. Kolesik, J. V. Moloney, and M. Mlejnek, Unidirectional Optical Pulse Propagation Equation, Phys. Rev. Lett. **89**, 283902 (2002).

[14] A. Couairon, E. Brambilla, T. Corti, D. Majus, O. Ramirez-Gongora, and M. Kolesik, Practitioner's guide to laser pulse propagation models and simulation, Eur. Phys. J.: Spec. Top. **199**, 5 (2011).

[15] V. Y. Fedorov, M. Chanal, D. Grojo, and S. Tzortzakis, Accessing Extreme Spatiotemporal Localization of High-Power Laser Radiation through Transformation Optics and Scalar Wave Equations, Phys. Rev. Lett. **117**, 043902 (2016).

[16] D. E. Shipilo, I. A. Nikolaeva, V. Y. Fedorov, S. Tzortzakis, A. Couairon, N. A. Panov, and O. G. Kosareva, Tight focusing of electromagnetic fields by large-aperture mirrors, Phys. Rev. E **100**, 033316 (2019).

[17] B. Chimier, O. Utéza, N. Sanner, M. Sentis, T. Itina, P. Lassonde, F. Légaré, F. Vidal, and J. C. Kieffer, Damage and ablation thresholds of fused-silica in femtosecond regime, Phys. Rev. B **84**, 094104 (2011).

[18] S. Mao, F. Quéré, S. Guizard, X. Mao, R. Russo, G. Petite, and P. Martin, Dynamics of femtosecond laser interactions with dielectrics, Appl. Phys. A **79**, 1695 (2004).

[19] C. Mézel, L. Hallo, A. Bourgeade, D. Hébert, V. T. Tikhonchuk, B. Chimier, B. Nkonga, G. Schurtz, and G. Travaillé, Formation of nanocavities in dielectrics: A self-consistent modeling, Phys. Plasmas **15**, 093 (2008).

[20] K. I. Popov, C. McElcheran, K. Briggs, S. Mack, and L. Ramunno, Morphology of femtosecond laser modification of bulk dielectrics, Opt. Express **19**, 271 (2011).

[21] N. M. Bulgakova, V. P. Zhukov, and Y. P. Meshcheryakov, Theoretical treatments of ultrashort pulse laser processing

of transparent materials: Toward understanding the volume nanograting formation and "quill" writing effect, Appl. Phys. B **113**, 437 (2013).

[22] R. Beuton, B. Chimier, P. Quinoman, P. González de Alaiza Martínez, R. Nuter, and G. Duchateau, Numerical studies of dielectric material modifications by a femtosecond Bessel–Gauss laser beam, Appl. Phys. A **127**, 334 (2021).

[23] F. Quéré, Etude des mécanismes d'excitation électronique associés au claquage des diélectriques induit par un champ laser intense, Ph.D. thesis, Université Paris 6, 2000.

[24] V. Mizeikis, S. Juodkazis, T. Balčiūnas, H. Misawa, S. I. Kudryashov, V. D. Zvorykin, and A. A. Ionin, Optical and ultrasonic signatures of femtosecond pulse filamentation in fused silica, J. Appl. Phys. **105**, 123106 (2009).

[25] T. V. Perevalov, V. A. Gritsenko, and V. V. Kaichev, Electronic structure of aluminum oxide: Ab initio simulations of α and γ phases and comparison with experiment for amorphous films, Eur. Phys. J. Appl. Phys. **52**, 30501 (2010).

[26] Y.-N. Xu and W. Y. Ching, Self-consistent band structures, charge distributions, and optical-absorption spectra in MgO, α-Al_2O_3, and $MgAl_2O_4$, Phys. Rev. B **43**, 4461 (1991).

[27] N. Naka, K. Fukai, Y. Handa, and I. Akimoto, Direct measurement via cyclotron resonance of the carrier effective masses in pristine diamond, Phys. Rev. B **88**, 035205 (2013).

[28] O. Herrfurth, T. Pflug, M. Olbrich, M. Grundmann, A. Horn, and R. Schmidt-Grund, Femtosecond-time-resolved imaging of the dielectric function of ZnO in the visible to near-IR spectral range, Appl. Phys. Lett. **115**, 212103 (2019).

[29] A. Rämer, O. Osmani, and B. Rethfeld, Laser damage in silicon: Energy absorption, relaxation, and transport, J. Appl. Phys. **116**, 053508 (2014).

[30] N. S. Grigoryan, T. Zier, M. E. Garcia, and E. S. Zijlstra, Ultrafast structural phenomena: Theory of phonon frequency changes and simulations with code for highly excited valence electron systems, J. Opt. Soc. Am. B **31**, C22 (2014).

[31] R. Ernstorfer, M. Harb, C. T. Hebeisen, G. Sciaini, T. Dartigalongue, and R. J. D. Miller, The formation of warm dense matter: Experimental evidence for electronic bond hardening in gold, Science **323**, 1033 (2009).

[32] A. Denoeud, A. Benuzzi-Mounaix, A. Ravasio, F. Dorchies, P. M. Leguay, J. Gaudin, F. Guyot, E. Brambrink, M. Koenig, S. Le Pape, and S. Mazevet, Metallization of Warm Dense SiO_2 Studied by XANES Spectroscopy, Phys. Rev. Lett. **113**, 116404 (2014).

[33] B. Rethfeld, D. Ivanov, M. Garcia, and S. Anisimov, Modelling ultrafast laser ablation, J. Phys. D **50**, 193001 (2017).

[34] S. Braginskii, Transport processes in a plasma, Rev. Plasma Phys. **1**, 205 (1965).

[35] J. A. Bittencourt, *Fundamentals of Plasma Physics* (Springer, New York, 2013).

[36] P. McKenna, D. Neely, R. Bingham, and D. Jaroszynski, *Laser-Plasma Interactions and Applications* (Springer, Berlin, 2013).

[37] D. L. Woolard, H. Tian, R. J. Trew, M. A. Littlejohn, and K. W. Kim, Hydrodynamic electron-transport model: Nonparabolic corrections to the streaming terms, Phys. Rev. B **44**, 11119 (1991).

[38] A. Hakim, J. Loverich, and U. Shumlak, A high resolution wave propagation scheme for ideal two-fluid plasma equations, J. Comput. Phys. **219**, 418 (2006).

[39] P. Mulser, F. Cornolti, and D. Bauer, Modeling field ionization in an energy conserving form and resulting nonstandard fluid dynamics, Phys. Plasmas **5**, 4466 (1998).

[40] E. T. Meier and U. Shumlak, A general nonlinear fluid model for reacting plasma-neutral mixtures, Phys. Plasmas **19**, 072508 (2012).

[41] A. Kaiser, B. Rethfeld, M. Vicanek, and G. Simon, Microscopic processes in dielectrics under irradiation by subpicosecond laser pulses, Phys. Rev. B **61**, 11437 (2000).

[42] D. Swanson, *Plasma Kinetic Theory* (CRC Press, Boca Raton, FL, 2008).

[43] P. L. Bhatnagar, E. P. Gross, and M. Krook, A model for collision processes in gases. I. Small amplitude processes in charged and neutral one-component systems, Phys. Rev. **94**, 511 (1954).

[44] B. Morel, R. Giust, K. Ardaneh, and F. Courvoisier, A simple solver for the two-fluid plasma model based on pseudospectral time-domain algorithm, Commun. Comput. Phys. **29**, 955 (2020).

[45] V. E. Golant, A. P. Zhilinsky, and I. E. Sakharov, *Fundamentals of Plasma Physics* (Wiley, New York, 1980).

[46] J. L. Delcroix and A. Bers, *Physique des plasmas* (EDP Sciences, Paris, 1994), Vol. 2.

[47] L. V. Keldysh, Ionization in the field of a strong electromagnetic wave, J. Exp. Theor. Phys. **20**, 1307 (1965).

[48] V. E. Gruzdev, Photoionization rate in wide band-gap crystals, Phys. Rev. B **75**, 205106 (2007).

[49] J. R. Peñano, P. Sprangle, B. Hafizi, W. Manheimer, and A. Zigler, Transmission of intense femtosecond laser pulses into dielectrics, Phys. Rev. E **72**, 036412 (2005).

[50] A. Couairon and A. Mysyrowicz, Femtosecond filamentation in transparent media, Phys. Rep. **441**, 47 (2007).

[51] B. K. Ridley, *Quantum Processes in Semiconductors* (Oxford University Press, Oxford, 2013).

[52] M. Garcia-Lechuga, L. Haahr-Lillevang, J. Siegel, P. Balling, S. Guizard, and J. Solis, Simultaneous time-space resolved reflectivity and interferometric measurements of dielectrics excited with femtosecond laser pulses, Phys. Rev. B **95**, 214114 (2017).

[53] R. F. Haglund and I. Itoh, *Laser Ablation: Principles and Applications* (Springer, Berlin, 1994).

[54] F. Quéré, S. Guizard, P. Martin, G. Petite, O. Gobert, P. Meynadier, and M. Perdrix, Ultrafast carrier dynamics in laser-excited materials: Subpicosecond optical studies, Appl. Phys. B **68**, 459 (1999).

[55] G. Petite, P. Daguzan, S. Guizard, and P. Martin, Ultrafast optical measurements of defect creation in laser irradiated SiO_2, J. Phys. III **6**, 1647 (1996).

[56] B. Morel, R. Giust, K. Ardaneh, and F. Courvoisier, A solver based on pseudo-spectral analytical time-domain method for the two-fluid plasma model, Sci. Rep. **11**, 3151 (2021).

[57] L. Rapp, R. Meyer, R. Giust, L. Furfaro, M. Jacquot, P.-A. Lacourt, J. Dudley, and F. Courvoisier, High aspect ratio micro-explosions in the bulk of sapphire generated by femtosecond Bessel beams, Sci. Rep. **6**, 34286 (2016).

[58] K. Ardaneh, R. Giust, B. Morel, and F. Courvoisier, Generation of a Bessel beam in FDTD using a cylindrical antenna, Opt. Express **28**, 2895 (2020).

[59] O. Shapoval, J. L. Vay, and H. Vincenti, Two-step perfectly matched layer for arbitrary-order pseudo-spectral analytical time-domain methods, Comput. Phys. Commun. **235**, 102 (2019).

[60] S. Juodkazis, K. Nishimura, and H. Misawa, In-bulk and surface structuring of sapphire by femtosecond pulses, Appl. Surf. Sci. **253**, 6539 (2007).

[61] K. Ardaneh, R. Meyer, M. Hassan, R. Giust, C. Xie, B. Morel, I. Ouadghiri-Idrissi, L. Furfaro, L. Froehly, A. Couairon, G. Bonnaud, and F. Courvoisier, A new route to high energy density inside the bulk of transparent materials, arXiv:2109.00803.

[62] K. Bennemann, Photoinduced phase transitions, J. Phys.: Condens. Matter **23**, 073202 (2011).

[63] T. Apostolova and B. Obreshkov, Femtosecond optical breakdown in silicon, Appl. Surf. Sci. **572**, 151354 (2022).

[64] W. Kruer, *The Physics of Laser Plasma Interactions* (Avalon, Boca Raton, 2003).

[65] D. Hulin, M. Combescot, J. Bok, A. Migus, J. Y. Vinet, and A. Antonetti, Energy Transfer during Silicon Irradiation by Femtosecond Laser Pulse, Phys. Rev. Lett. **52**, 1998 (1984).

[66] P. Balling and J. Schou, Femtosecond-laser ablation dynamics of dielectrics: Basics and applications for thin films, Rep. Prog. Phys. **76**, 036502 (2013).

[67] A. Mouskeftaras, S. Guizard, N. Fedorov, and S. Klimentov, Mechanisms of femtosecond laser ablation of dielectrics revealed by double pump-probe experiment, Appl. Phys. A **110**, 709 (2013).